The Astrophysical Journal, 897:161 (15pp), 2020 July 10 https://doi.org/10.3847/1538-4357/ab9810

Atmospheric Erosion by Giant Impacts onto Terrestrial Planets

J. A. Kegerreis[1], V. R. Eke[1], R. J. Massey[1], and L. F. A. Teodoro[2,3]
[1] Institute for Computational Cosmology, Durham University, Durham, DH1 3LE, UK; jacob.kegerreis@durham.ac.uk
[2] BAERI/NASA Ames Research Center, Moffett Field, CA, USA
[3] School of Physics and Astronomy, University of Glasgow, G12 8QQ, Scotland, UK
Received 2020 February 7; revised 2020 May 27; accepted 2020 May 28; published 2020 July 15

Abstract

We examine the mechanisms by which the atmosphere can be eroded by giant impacts onto Earth-like planets with thin atmospheres, using 3D smoothed particle hydrodynamics simulations with sufficient resolution to directly model the fate of low-mass atmospheres. We present a simple scaling law to estimate the fraction lost for any impact angle and speed in this regime. In the canonical Moon-forming impact, only around 10% of the atmosphere would have been lost from the immediate effects of the collision. There is a gradual transition from removing almost none to almost all of the atmosphere for a grazing impact as it becomes more head-on or increases in speed, including complex, nonmonotonic behavior at low impact angles. In contrast, for head-on impacts, a slightly greater speed can suddenly remove much more atmosphere. Our results broadly agree with the application of 1D models of local atmosphere loss to the ground speeds measured directly from our simulations. However, previous analytical models of shock-wave propagation from an idealized point-mass impact significantly underestimate the ground speeds and hence the total erosion. The strong dependence on impact angle and the interplay of multiple nonlinear and asymmetrical loss mechanisms highlight the need for 3D simulations in order to make realistic predictions.

Unified Astronomy Thesaurus concepts: Earth atmosphere (437); Planetary atmospheres (1244); Impact phenomena (779); Hydrodynamical simulations (767)

1. Introduction

Terrestrial planets are thought to form from tens of roughly Mars-sized embryos that crash into each other after accreting from a protoplanetary disk (Chambers 2001). At the same time, planets grow their atmospheres by accreting gas from their surrounding nebula, degassing impacting volatiles directly into the atmosphere, and outgassing volatiles from their interior (Massol et al. 2016).

For a young atmosphere to survive it must withstand radiation pressure of its host star, frequent impacts of small and medium impactors, and typically at least one late giant impact that could remove an entire atmosphere in a single blow (Schlichting & Mukhopadhyay 2018). In this paper, we focus on the direct, dynamical consequences of giant impacts onto planets like the early Earth.

Our own planet is a compelling example, since we can both observe an atmosphere that has survived to the present day and be confident that a giant impact took place late in its evolution —creating the Moon in the process. Several different Moon-formation scenarios have been proposed and revised, but no simulations have yet resolved a crust, ocean, or atmosphere for the proto-Earth (e.g., Ćuk & Stewart 2012; Lock et al. 2018).

Focusing on the atmosphere, Earth's volatile abundances are remarkably different from those of chondrites (Halliday 2013), which act as a record of the condensable components of the early solar system. Specifically, nitrogen and carbon are depleted compared with hydrogen, which could be explained by the loss of N_2 and CO_2 with an eroded atmosphere while retaining H_2O in an ocean (Sakuraba et al. 2019). Unlike the abundances, the isotope ratios match those of primordial chondrites. Hydrodynamic escape—driven by XUV radiation from the star or heat from the planet below—preferentially removes lighter isotopes, while impacts remove bulk volumes of atmosphere. This suggests that impacts (not necessarily giant ones) are the primary loss mechanism, driving fractionation by removing more atmosphere than ocean while preserving isotope ratios (Schlichting & Mukhopadhyay 2018).

Furthermore, the relative abundances of helium and neon in different-aged mantle reservoirs suggest that Earth lost its atmosphere on at least two occasions (Tucker & Mukhopadhyay 2014). Fractionation of xenon also indicates a complicated history of atmospheric loss and the importance of ionic escape in addition to impact erosion and hydrodynamic escape (Zahnle et al. 2019).

Looking farther afield, we have recently learned not only that Earth- to Neptune-mass exoplanets are common but also that they host a remarkable diversity of atmospheric masses (Fressin et al. 2013; Petigura et al. 2013; Lopez & Fortney 2014). The stochastic nature of giant impacts makes them a strong candidate for explaining some of the differences between planets that would otherwise be expected to have evolved similarly (Liu et al. 2015; Bonomo et al. 2019). Irradiation and photoevaporation from stellar winds can significantly erode an atmosphere (Lopez et al. 2012; Zahnle & Catling 2017), but not enough to explain the diversity of planets around dim stars, where it should be much less effective.

Previous studies of giant impact erosion have primarily used analytical approaches and 1D simulations to estimate atmospheric loss from a range of impact energies (e.g., Genda & Abe 2003; Inamdar & Schlichting 2015). The one-dimensional nature of these studies also means that little work has been done on grazing collisions, in spite of the fact that these are far more likely to occur. Some studies have investigated oblique impacts for much smaller (of order 10 km) objects (Shuvalov 2009), in which case the erosion is only ever in the local region and the planet's curvature is negligible. Their results showed a strong increase in local loss for more oblique impacts, which is

the opposite of the trend for giant impacts (Kegerreis et al. 2018). The typical approach for giant impacts is to estimate the ground velocities induced by the impact to study how much atmosphere is blown away. This misses the complex details of a collision that can mix, deform, and remake both an atmosphere and the rest of the planet. Any precise study of the consequences of a giant impact therefore requires full 3D modeling of the planet and atmosphere at the same time.

Recent progress has been made in the regime of thick atmospheres by two studies: one with 3D simulations of head-on collisions of large super-Earths targeted at explaining a specific exoplanet system (Liu et al. 2015), and another with highly grazing impacts that do not make the solid layers of the planets interact (Hwang et al. 2018). This leaves serious gaps in our understanding of the formation and atmospheric evolution of planets in and outside the solar system, in terms of both lower atmosphere masses and the effect of the impact angle.

The aim of this study is thus to begin the exploration of this almost uncharted parameter space, starting in the regime of thin atmospheres. For example: what does the impactor actually do to remove atmosphere in different scenarios? How easy it is to partially erode some atmosphere as opposed to all or none? And how do these answers change for head-on, grazing, slow, or fast impacts?

Giant impacts are most commonly studied using smoothed particle hydrodynamics (SPH) simulations, where planets are modeled with particles that evolve under gravity and material pressure. It was recently shown that at least 10^7 (equal-mass) SPH particles can be required to converge on even the large-scale results from simulations of giant impacts, and that the resolution requirements for reliable results depend strongly on the specific scenario and question (Hosono et al. 2017; Kegerreis et al. 2019).

Computational advances enable us for the first time to study the erosion of thin atmospheres with full, 3D simulations. In this paper, we present high-resolution simulations of giant impacts with a variety of impact angles and speeds onto the proto-Earth, hosting a range of low atmosphere masses. We study the detailed mechanisms of erosion, compare with previous analytical and 1D estimates, and present a simple scaling law for the fraction of lost atmosphere in this regime.

2. Methods

In this section we describe the initial conditions for the model planets, the range of impact scenarios, and the previous models to which we compare our results. The SPH simulations are run using the hydrodynamics and gravity code SWIFT[4] (Schaller et al. 2016; Kegerreis et al. 2019).

2.1. Initial Conditions

As a recognizable starting point, we consider an impact similar to a canonical Moon-forming scenario, with a target proto-Earth of mass $0.887\,M_\oplus$ and impactor of mass $0.133\,M_\oplus$. Both are differentiated into an iron core and rocky mantle, constituting 30% and 70% of the total mass, respectively, and have no pre-impact rotation. The radii of the outer edge of the core and mantle are 0.49 and $0.96\,R_\oplus$ for the target and 0.29 and $0.57\,R_\oplus$ for the impactor. We use the simple Tillotson (1962) iron and granite equations of state (EOSs; Melosh 2007, Table AII.3) to model these materials (Kegerreis et al. 2019).[5]

For the atmospheres, we use the Hubbard & MacFarlane (1980) hydrogen–helium EOS, as described in Kegerreis et al. (2018). This includes a temperature- and density-dependent specific heat capacity and an adiabatic temperature–density relation. An ideal gas would probably be sufficient for the smaller atmospheres, but larger ones stray into the denser regime that this EOS is designed to include.

The Tillotson EOS does not treat phase boundaries or mixed phases correctly but is widely used for SPH impact simulations owing to its computationally convenient analytical form (Stewart et al. 2019). These limitations could be important for studies that require accurate modeling of, for example, the thermodynamic state of low-density material in orbit. However, for the focus in this paper on the large-scale shock-wave propagation and overall erosion caused by impacts, the details of the EOS are not expected to significantly affect the results.

The atmosphere is adiabatic above a 500 K surface, while the iron and silicate layers are given a simple temperature–density relation of $T \propto \rho^2$, chosen somewhat arbitrarily to produce a central temperature of $\sim$5000 K similar to Earth today. Our surface temperature is lower than the 1500 K of Genda & Abe (2003), but the fact that their erosion results are similar to those of Inamdar & Schlichting (2015) that used many thousands of kelvin suggests that the loss is not highly sensitive to this choice, as we test directly ourselves in Section 3.3.

We test a range of atmosphere masses on the proto-Earth, namely, 10^{-1}, $10^{-1.5}$, 10^{-2}, and $10^{-2.5}\,M_\oplus$, as the lowest mass that we might expect to resolve adequately with 10^7 equal-mass SPH particles. The corresponding pressure at the base of the atmosphere is 5.5, 2.4, 0.92, and 0.32 GPa, respectively. They extend out to a pressure of $\sim$0.1 MPa at 1.55, 1.27, 1.13, and $1.06\,R_\oplus$, respectively. Earth's atmosphere today has a mass of $\sim 10^{-6}\,M_\oplus$, though it may have been much thicker in the past.

To produce the radial density and temperature profiles for each atmosphere mass, the surface temperature is kept fixed at 500 K for simplicity, while the surface pressure is varied until the desired atmospheric mass is obtained. In other words, the inner two layer profiles are integrated inward from the surface (see Kegerreis et al. 2019, Appendix A), and then the atmosphere layer profile is integrated outward, until reaching a negligible minimum density of $10\,\mathrm{kg\,m^{-3}}$. Separately, the total radius is also iterated to obtain the 30:70 mass ratio of iron to rock.

Particles are then placed to precisely match these profiles using the stretched equal-area (SEA) method[6] described in Kegerreis et al. (2019). This results in a relaxed arrangement of particles that have SPH densities within 1% of the desired profile values, mitigating the need for extra computation that is otherwise required to produce initial conditions that are settled and ready for a simulation.

2.2. Impact Simulations

We specify each impact scenario by the impact parameter, $b = \sin(\beta)$, and the speed, v_c, at first contact of the impactor with the target's surface, as illustrated in Figure 1. The initial

[4] SWIFT is in open development and publicly available at www.swiftsim.com.

[5] Note that Appendix B of Kegerreis et al. (2019) has a typo in the sign of $\mathrm{d}u = T\mathrm{d}S - P\mathrm{d}V = T\mathrm{d}S + (P/\rho^2)\,\mathrm{d}\rho$ just after Equation (B1).

[6] The SEAGen code is publicly available at github.com/jkeger/seagen, and the python module `seagen` can be installed directly with pip.

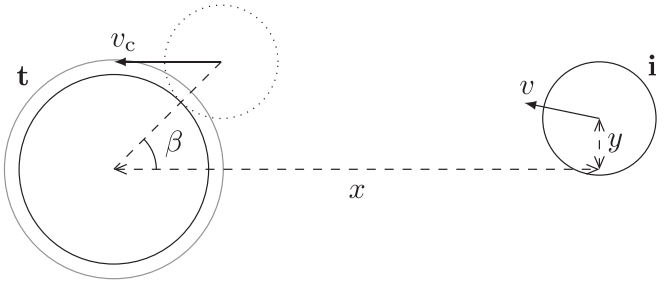

Figure 1. Initial conditions for an impact scenario, with the target (t) on the left and the impactor (i) on the right, in the target's rest frame. The angle of first contact, β, is set ignoring the atmosphere and neglecting any tidal distortion before the collision. The initial separation is set by the time to impact, as described in Appendix A.

position of the impactor is set such that contact occurs 1 hr after the start of the simulation, to allow for some natural tidal distortion and to not disrupt the system by suddenly introducing the large impactor right next to the no-longer-in-equilibrium target, as described in Appendix A. Note that the speed at contact is always chosen in units of the mutual escape speed of the system, $v_{esc} = \sqrt{2G(M_t + M_i)/(R_t + R_i)}$, where R_t neglects the thickness of any atmosphere, which is slightly faster for the planets with more massive atmospheres (from 9.1 up to 9.6 km s^{-1}).

We run a primary suite of 74 simulations with $\sim 10^7$ SPH particles, plus 10 of these scenarios resimulated additionally with 10^6, $10^{6.5}$, $10^{7.5}$, and 10^8 particles for convergence tests, plus 12 miscellaneous tests with 10^7 particles detailed in Section 3.3. To be precise, these stated particle numbers refer to the number of particles per Earth mass (the bare target plus impactor mass is 1.02 $M_\oplus$). Thus, the numerical resolution stays the same for simulations with different-mass planets. For example, a "10^7" simulation that includes a 0.1 $M_\oplus$ atmosphere actually contains a total of $\sim 1.12 \times 10^7$ particles. For most of the suite we focus on the 10^{-2} $M_\oplus$ atmosphere.

Figure 2 summarizes the parameters for each simulation. Note that the $v_c = 0.75\, v_{esc}$ scenarios would require some third body to have slowed down the impactor during its approach to below the mutual escape speed. This is unlikely in the case of primary impactors falling in to Earth in our solar system but is a useful test for the consequences of a highly grazing impact resulting in a large bound fragment that will re-impact at a later time. It also lets us compare with other models, which predict little erosion in this regime.

At the high-speed end, given Earth's position in the solar system, $5v_{esc}$ is around the highest typical velocity that might be expected for an impact (Raymond et al. 2009). For context, Earth's orbital speed around the Sun is about $3v_{esc}$. The suite's extension to $8v_{esc}$ both allows us to test the extreme end of the parameter space and is a regime that could be more common in other planetary systems, for example, with a more massive star or a target planet deeper in the star's potential well. Furthermore, in studies like that by Inamdar & Schlichting (2015) where erosion is estimated as a function of the impactor's momentum, using very high velocities will allow us to test the degeneracy between impactor mass and speed across a wide range of momenta in future suites with different impactor masses. For the relatively small impactor mass used here, even $8v_{esc}$ is not predicted by Inamdar & Schlichting (2015) to remove more than 3/4 of the atmosphere.

The simulations are run using SWIFT with a simple "vanilla" form of SPH plus the Balsara (1995) switch for the artificial viscosity as described in Kegerreis et al. (2019) to a simulation

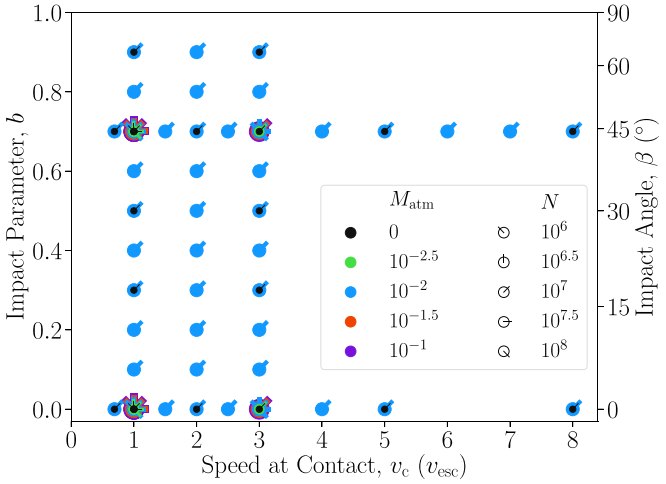

Figure 2. Suite of simulation scenarios, arranged by their speed and impact parameter at contact (see Figure 1 and Appendix A). As shown in the legend, the nested marker colors indicate the mass of the atmosphere (in Earth masses) for each simulation, while the line angles indicate the number of particles per Earth mass.

time of 100,000 s (roughly 28 hr) in a cubic box of side 80 $R_\oplus$ to allow the tracking of ejecta. Any particles that leave the box are removed from the simulation. Throughout the first 10 hr we record snapshots every 100 s, for high time resolution during the impact and its immediate aftermath. To reduce data storage requirements, we then output snapshots every 1000 s for the remainder.

2.3. Analytical and 1D Models

We use two previous erosion studies for comparison with our 3D simulations, both for the resulting loss of atmosphere and for the shock waves caused by the impact. Genda & Abe (2003) used 1D models to simulate the reaction of the atmosphere to a shock from vertical ground motion. Their results for the local fraction of lost atmosphere, X_{local}, are fitted well by a simple linear function of the ground speed, v_{gnd}, in units of the escape velocity: $X_{local} = -1/3 + 4/3\ (v_{gnd}/v_{esc})$ capped at zero and one (their Equation (17)), which they conclude is largely insensitive to the initial conditions of the atmosphere.

Inamdar & Schlichting (2015) performed similar 1D, Lagrangian, vertical-shock simulations but extended them to include thicker atmospheres up to 10% of the solid mass of the planet. They agree with Genda & Abe (2003) for thin atmospheres. Schlichting et al. (2015) also created a model for predicting the ground speeds caused by a giant impact, by treating the collision as a point-mass explosion on a spherical planet of constant density. They assumed momentum conservation with a uniform speed in the spherical region traversed by the shock front, which leads to the vertical ground speed as a function of distance, l, from the impact point: $v_{gnd} = v_{imp}(M_i/M_t)\ [(l/(2R_t))^2(4 - 3l/(2R_t))]^{-1}$ (their Equation (28)), where v_{imp} is the speed of the impactor and R_t and M_t are the radius and mass of the target planet, respectively. By combining their speed estimates with the 1D local erosion model, they presented predictions for the global atmospheric mass-loss fraction as a function of the impactor speed and velocity for different atmosphere masses (their Figure 5).

3. Results and Discussion

We begin investigating the simulations with an overview of the general features and consequences of these classes of impacts. Then, we focus on the isolated effects of changing the impact parameter, speed, or atmosphere mass and examine the

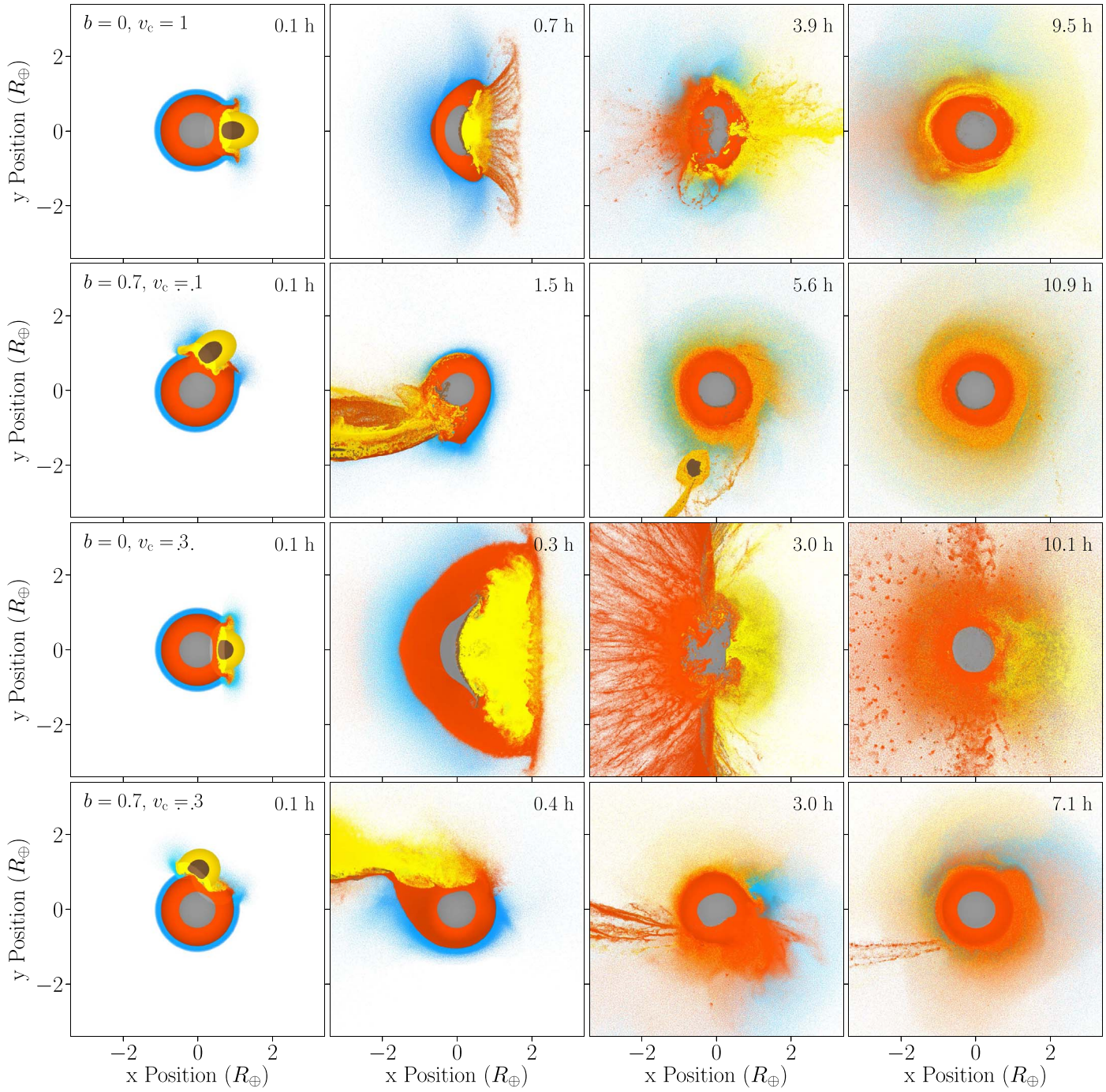

Figure 3. Illustrative early snapshot cross sections from the four fiducial impact simulations—head-on and slow, grazing and slow, head-on and fast, grazing and fast—with $b = 0$ or 0.7, and $v_c = 1$ or 3 (labeled throughout in units of v_{esc}), with the 1% $M_\oplus$ atmosphere and $\sim 10^8$ SPH particles. Gray and orange show the target's core and mantle material, respectively, and brown and yellow show the same for the impactor. Blue is the target's atmosphere. The color luminosity varies slightly with the internal energy. Note that the snapshots are at different times for each simulation to show the evolution in each case. The impactors are traveling in the $-x$-direction at the moment they contact the target (see Figure 1). Animations of the early evolution of these impacts are available at icc.dur.ac.uk/giant_impacts.

time at which material is ejected. We consider the ground speeds and localized loss to compare our results with previous estimates, and then we collate all the simulation results to find a simple scaling law for the total atmospheric erosion from any scenario in this regime.

3.1. General Features of Impacts and Erosion

We choose four simulations to act as fiducial comparisons for the rest of the suite, demonstrating head-on and grazing, slow and fast scenarios. They stand out in Figure 2 as the impacts for which we simulate multiple atmosphere masses and with multiple resolutions. Snapshots from these fiducial simulations are shown in Figure 3, for a target with a 1% $M_\oplus$ atmosphere, using $\sim 10^8$ SPH particles.

In general, the impactor merges with the target for head-on or slow cases but may not for fast, grazing impacts. In addition to any differences in the resulting fraction of lost atmosphere, the timing and cause of loss can also vary significantly with the impact scenario. For example, atmosphere may be eroded by the following, in approximately chronological order:

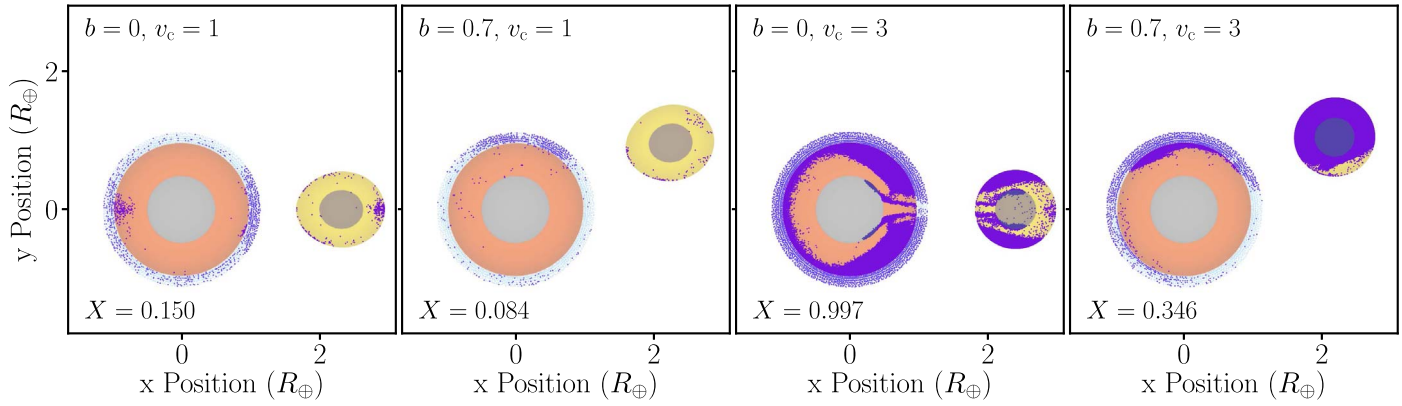

Figure 4. Particles that will become unbound and escape the system, highlighted in purple on a pre-impact snapshot, for the four fiducial impacts and our standard $\sim 10^7$ SPH particles. The other particle colors are muted versions of those in Figure 3 as a background for the highlighted ones. Only a thin cross section of the particles that are within one SPH smoothing length of $z = 0$ are shown for clarity. For grazing impacts, higher latitudes may suffer less erosion (see Section 3.4). The X values give the total mass fraction of the atmosphere that is lost.

1. Direct encounter with the very-much-not-a-point-mass impactor passing through, most dramatically demonstrated in the high-speed, grazing case (fourth row).
2. The shock wave traveling through the planet from the impact point, which even erodes some mantle as well in the high-speed, head-on case (third row).
3. Subsequent oscillations of the planet, such as the plume of impactor mantle in the third snapshot of the low-speed, head-on case (first row)—much like the large splash created after dropping a stone into a pond.
4. The secondary impact of the impactor following an initial grazing collision, as in the third snapshot of the low-speed, grazing case (second row).

All of these mechanisms may contribute to the total loss in a given scenario. This provides some context with which to consider the rest of the suite and some appreciation for the complexity created by all these processes intermingling.

The particles that are eroded by these four impacts are highlighted in Figure 4, selected by being gravitationally unbound and remaining so until the end of the 10^5 s simulation or until the time the particle exits the $80\,R_\oplus$-wide simulation box. The resulting mass fractions of lost atmosphere are 0.15, 0.08, 1.0, and 0.39, respectively. We revisit these final loss results in the context of the whole suite after presenting the rest of the simulations and introducing the previous analytical and 1D estimates for comparison. For now, Figure 4 demonstrates the expected qualitative results following the above discussion of Figure 3: the head-on, slow case loses atmosphere around the impact point and the antipode; the grazing, slow case shows little antipode erosion, suggesting a weaker shock, and primarily loses atmosphere in the direct path of the impactor; the head-on, fast impactor has blasted off almost all the atmosphere and some mantle from the strong shock wave; and the grazing, fast case is similar to the grazing, slow one, but the impactor has taken some of the mantle in its path along with the atmosphere and blasted away some atmosphere around the antipode. The grazing, fast impactor itself also remains unbound in this hit-and-run collision.

Note that even head-on collisions are not *perfectly* rotationally symmetric in our simulations, because the system is represented using a finite number of particles. For example, in addition to the large plume of material ejected during the low-speed, head-on impact, a small blast occurs on the $-y$ side (first row in Figure 3). This is impactor material that initially plunges deep into the target's center. Being much less dense than the iron core, it gets rapidly forced back out in a random direction determined by the arrangement of the discrete particles. In our simulations of the same impact scenario using different numbers of particles, the same eruption of material is produced at the same time, but with different random orientations in the y–z plane. On the one hand, this highlights the imperfect symmetry of our SPH planets, which prevents the modeling of perfectly idealized head-on collisions. On the other hand, this also demonstrates the importance of using fully 3D hydrodynamical simulations to study realistically chaotic giant impacts, where we should expect some level of asymmetry and precisely head-on impacts have a probability of zero. At any rate, this feature ejects negligible unbound material, so it does not affect the overall results of this specific study.

We now turn to the rest of the suite in a similar manner, continuing this initial overview of general behavior. The top two rows of Figure 5 highlight the particles that become lost from subsets of changing impact-parameter scenarios, with either the low or high fiducial speeds and the same atmosphere and number of particles. Filling in the gaps between the fiducial examples, there is a trend from more global, shock-driven erosion for low impact parameters to direct, localized erosion for high impact parameters.

The bottom two rows of Figure 5 show the eroded particles from subsets of changing speed scenarios, with either the head-on or grazing fiducial impact parameters. Even though the slowest impactors make contact at below the escape speed, they still erode some atmosphere locally. For head-on impacts, by $v_c = 2v_{esc}$, already almost all of the atmosphere is eroded. At higher speeds, more mantle is also lost, and $v_c = 8v_{esc}$ disintegrates the planet entirely. The faster grazing impacts can still deliver enough energy to drive some antipodal loss but remove systematically less atmosphere than head-on collisions, and even by $v_c = 5v_{esc}$ with $b = 0.7$ almost half of the atmosphere still survives.

We find broadly similar behavior for different masses of atmosphere, in simulations with the same fiducial impact parameters and speeds. For slow, head-on impacts onto targets with atmospheres at and below $\sim 10^{-2}\,M_\oplus$, the mantle erosion is similar to the case with zero atmosphere. Thicker atmospheres begin to significantly cushion the mantle from erosion. The low- and zero-mass atmosphere cases are also similar in

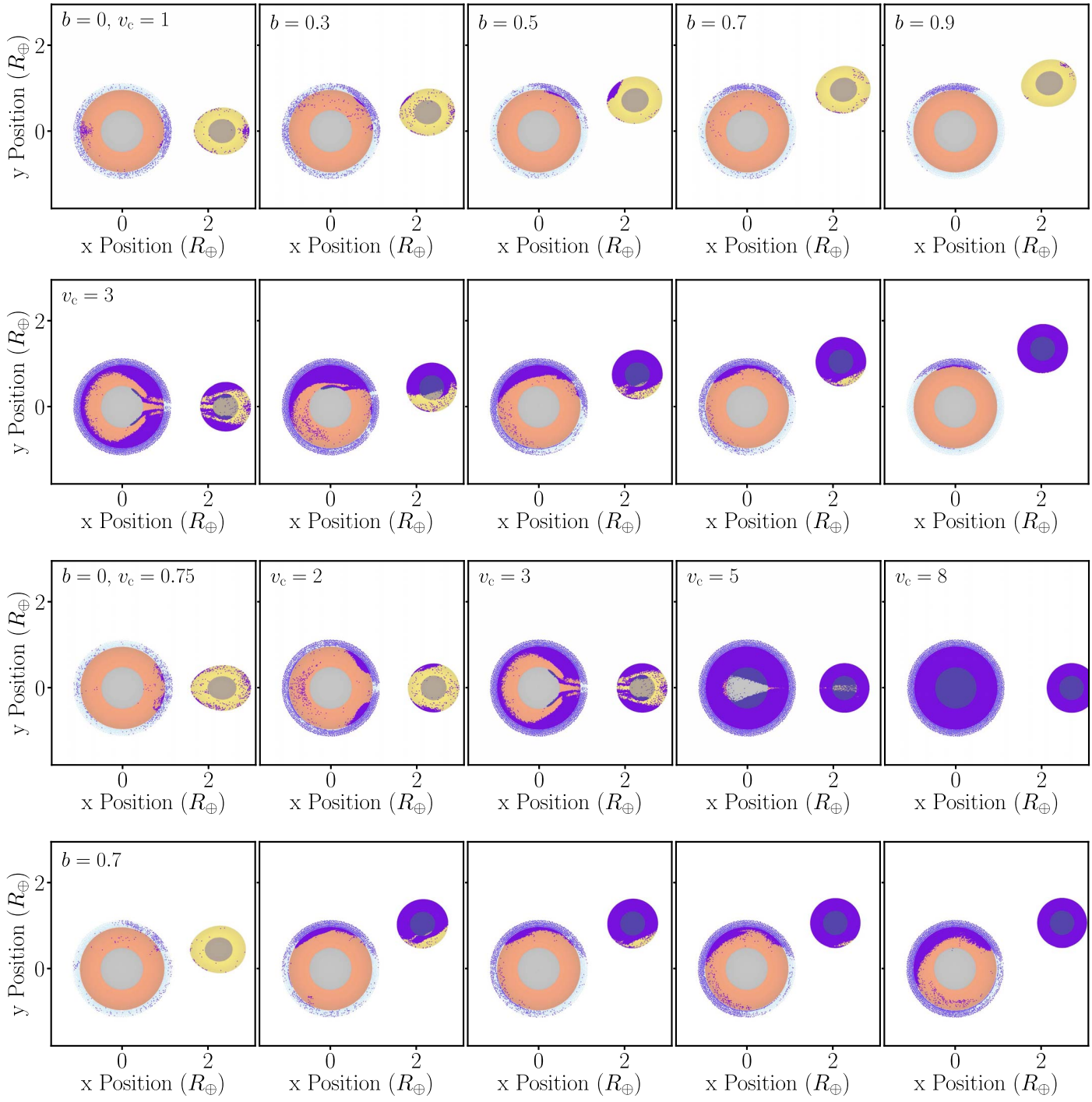

Figure 5. Particles that will become unbound and escape the system, as in Figure 4, for example subsets of different impact parameters (top two rows) and different speeds at contact (bottom two rows).

the other three fiducial scenarios, although for slow, grazing collisions the thicker atmospheres can affect the path of the impactor as it passes through, making the comparison less direct. At higher speeds, the atmosphere mass makes less difference, especially in the head-on case, because both any gravitational acceleration and hydrodynamical deceleration will have smaller effects.

3.2. Erosion Time Evolution

The time at which the lost atmosphere becomes unbound is shown in Figure 6, for subsets of changing impact parameter and changing speed scenarios. Significant atmosphere can be eroded after the initial impact, especially for slower collisions with low impact parameters. This corresponds to the potentially violent oscillations of the planet, shocking away surviving shells of atmosphere or even ejecting plumes of material, as seen in the slow, head-on fiducial example (Figure 3). For high impact parameters, delayed erosion can also be caused by the secondary collision of grazing impactor fragments. However, given the low speeds required for a grazing fragment to return and the likely reduced mass of the fragment, this has a smaller effect.

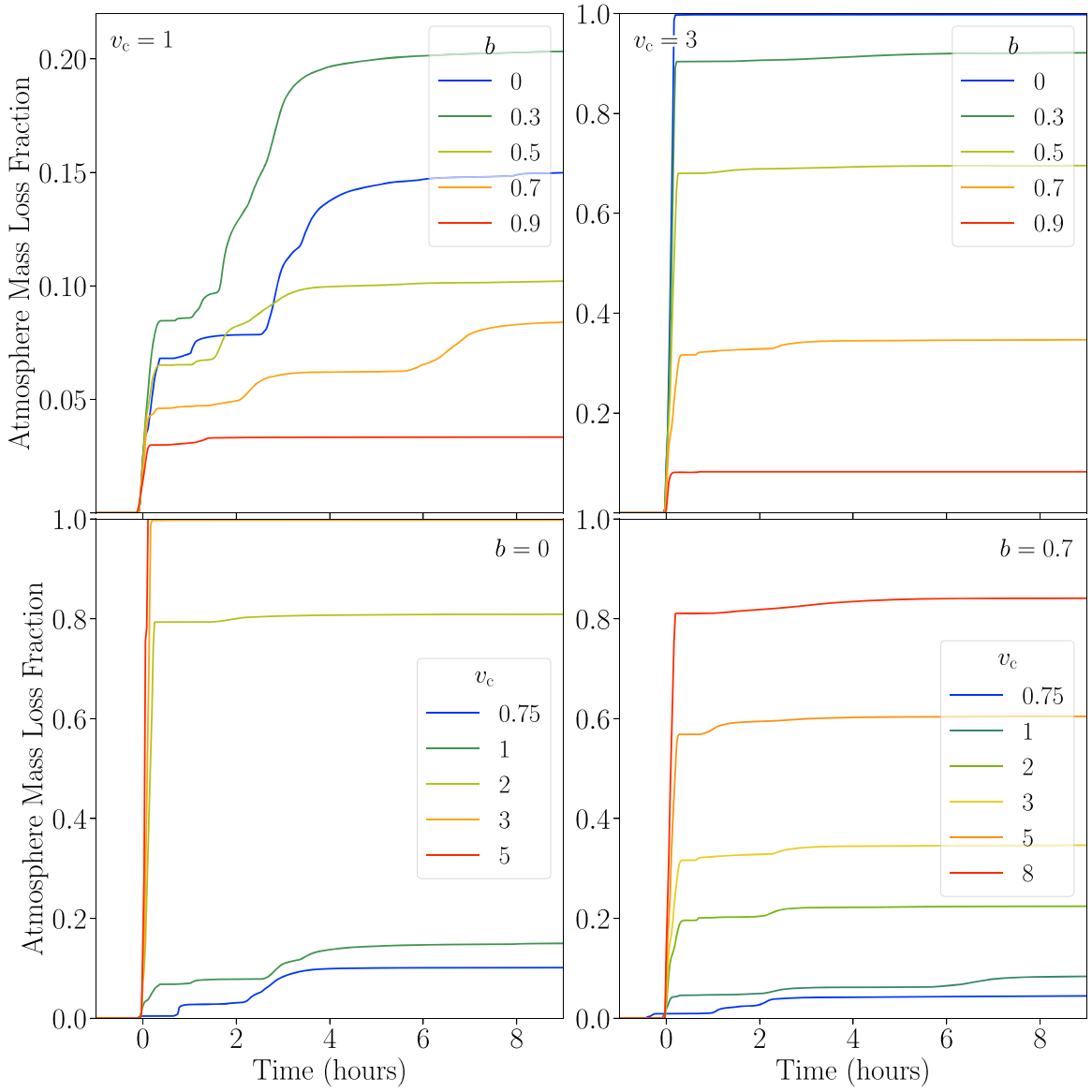

Figure 6. Early time evolution of the mass fraction of unbound atmosphere for different subsets of impact parameters and speeds (labeled in units of v_{esc}) with the 1% $M_\oplus$ atmosphere and $\sim 10^7$ particles. i.e., the times at which the highlighted atmosphere particles in Figure 5 become unbound. Note that the vertical axis in the top left panel does not reach 1. Time = 0 is set to be the time of contact from Appendix A, 1 hr after the start of the simulation.

The majority of loss has finished by 4–8 hr after contact in all cases, and the eroded mass remains constant to within a few percent up to the end of the 28 hr simulations. For impact speeds of $\gtrsim 2 v_{esc}$, the erosion is completed almost immediately, with little change after only the first couple of hours. For low impact parameters, this is simply because the entire atmosphere is blown away by the initial shock. For grazing collisions, it is the lack of re-impacting fragments that reduces any later erosion.

Figure 7 shows the time evolution for the loss of the different-mass atmospheres. The qualitative evolution is similar in most cases, especially for the 10^{-2} and $10^{-2.5}\,M_\oplus$ atmospheres, and the total loss fraction is systematically lower for the thicker atmospheres. The drag of the atmosphere as the impactor passes through can reduce the erosion both immediately and by mitigating subsequent oscillations and secondary impacts. For the faster collisions, as before, the behavior remains comparatively simple with more immediate erosion and the results are less affected by the atmosphere's mass in terms of timing.

3.3. Convergence and Other Tests

To study the results of using different particle numbers, we duplicated each of the two slower fiducial simulations and the $10^{-2}\,M_\oplus$-atmosphere fast ones with 10^6, $10^{6.5}$, $10^{7.5}$, and 10^8 SPH particles (per Earth mass). For this initial project, we used 10^7 particles for the main suite to explore this new parameter space. Kegerreis et al. (2019) showed that 10^7 particles are approximately the minimum number required to resolve all of the major processes in sufficient detail. That being said, for the atmospheric erosion tests specifically (for thicker atmospheres than here), lower particle numbers still yielded results within 10% of the converged value.

Figure 7 shows that the number of particles required for convergence clearly depends on the scenario in addition to the atmosphere mass. The thicker atmospheres appear well converged by only $10^{6.5}$ particles, as are the $10^{-2}\,M_\oplus$ atmospheres for the high-speed scenarios. For the thinner atmospheres in the slower scenarios, the final results differ by a few percent even between

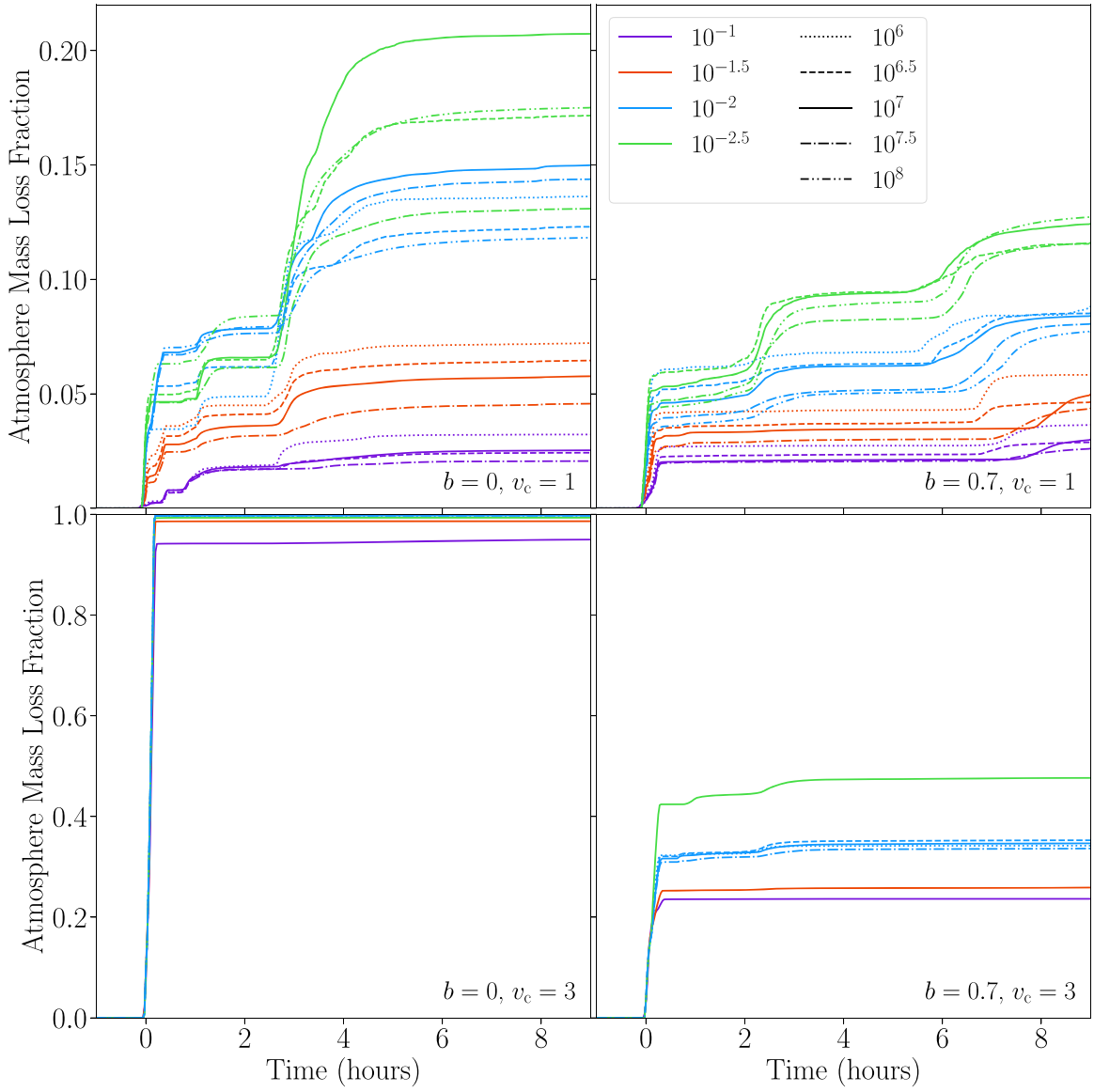

Figure 7. Early time evolution of the mass fraction of unbound atmosphere for the four fiducial impact scenarios with different atmosphere masses (labeled in units of $M_{\oplus}$). Note that the vertical axes in the top panels do not reach 1. The dotted and dashed lines show the loss evolution for different numbers of particles, as given in the legend.

$10^{7.5}$ and 10^{8} particles. As found by Kegerreis et al. (2019), the discrepancies manifest primarily after the initial impact, when debris falls back in and other smaller-scale processes can affect the overall results. Furthermore, regions where the atmosphere is only partially lost require many layers of particles to resolve, which is exacerbated when additional atmosphere is eroded multiple times after the initial shock. While this lack of perfect convergence is important to note, we can constrain the resulting systematic uncertainty for the loss fraction across the suite of $10^{-2}\,M_{\oplus}$ atmospheres to around 2% in slow scenarios and much smaller in more violent cases.

In order to further test the dependence of our results on the type of finite-particle issues discussed in relation to the slow, head-on collision in the first row of Figure 3, we ran 10 duplicate simulations with the target rotated to different orientations. Most of the resulting loss fractions agree to within a few percent of the mean of 0.47. However, three produced ∼0.07 more fractional erosion and one a remarkable 0.21 less, giving a standard deviation of 0.08. The qualitative evolution appears much the same in all 10 cases, but the details of the fallback and sloshing that follows the initial impact and rebound (see Figure 7) can differ significantly in magnitude. This chaotic behavior also helps to explain the incomplete convergence of the slow, head-on collisions discussed above. In contrast, similar rotated resimulations of fast, grazing impacts produced the same results consistently, indicating that these issues are restricted to the most sensitive slow, head-on cases. Therefore, we warn that significant care must be taken when interpreting the results from one-off simulations of slow, head-on impacts, even at high resolution.

We ran two additional tests with higher surface temperatures of 1000 and 2000 K on the target in an otherwise unchanged fast, grazing impact. The resulting loss fractions were 0.04 and 0.07 higher than the original result of 0.52, respectively. While the warmer atmospheres with their greater scale heights are indeed lost slightly more easily, this provides additional confidence that it is only a minor effect.

We also reran the same fast, grazing impact with a target mantle made of basalt (Benz & Asphaug 1999, Table II),

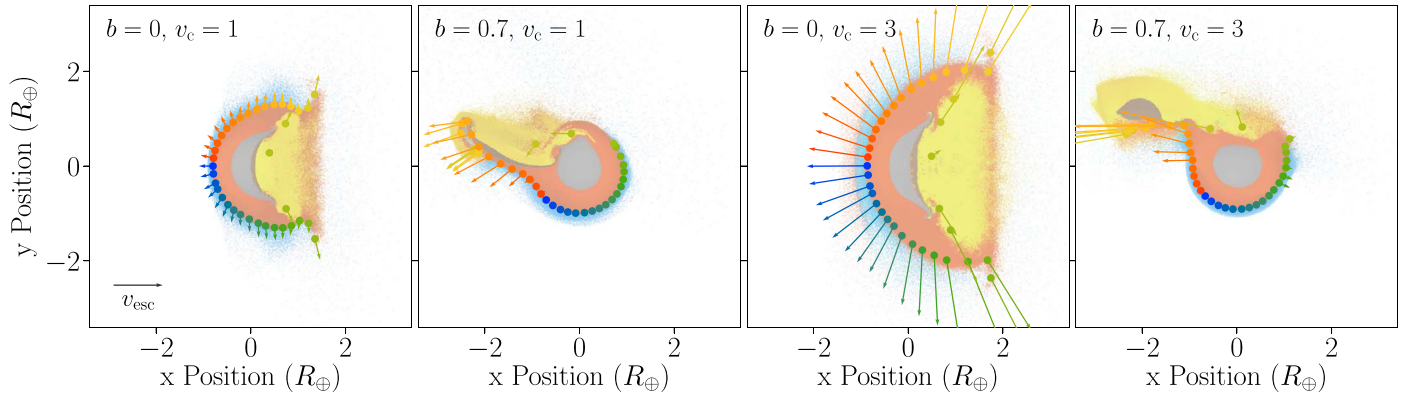

Figure 8. Example positions and velocities of the outermost "ground" particles of the target's mantle, for the four fiducial simulations at 0.4, 0.6, 0.2, and 0.2 hr after contact, respectively. The colors show the particles' original longitudes in bins of 10°, from 0° (pale green) at the point of contact to 180° (red) and −180° (blue) at the antipode, here within ±5° latitude of the 0° impact plane. The maximum speeds in Figure 10 are taken from across all snapshot times, whereas only single snapshots are shown here.

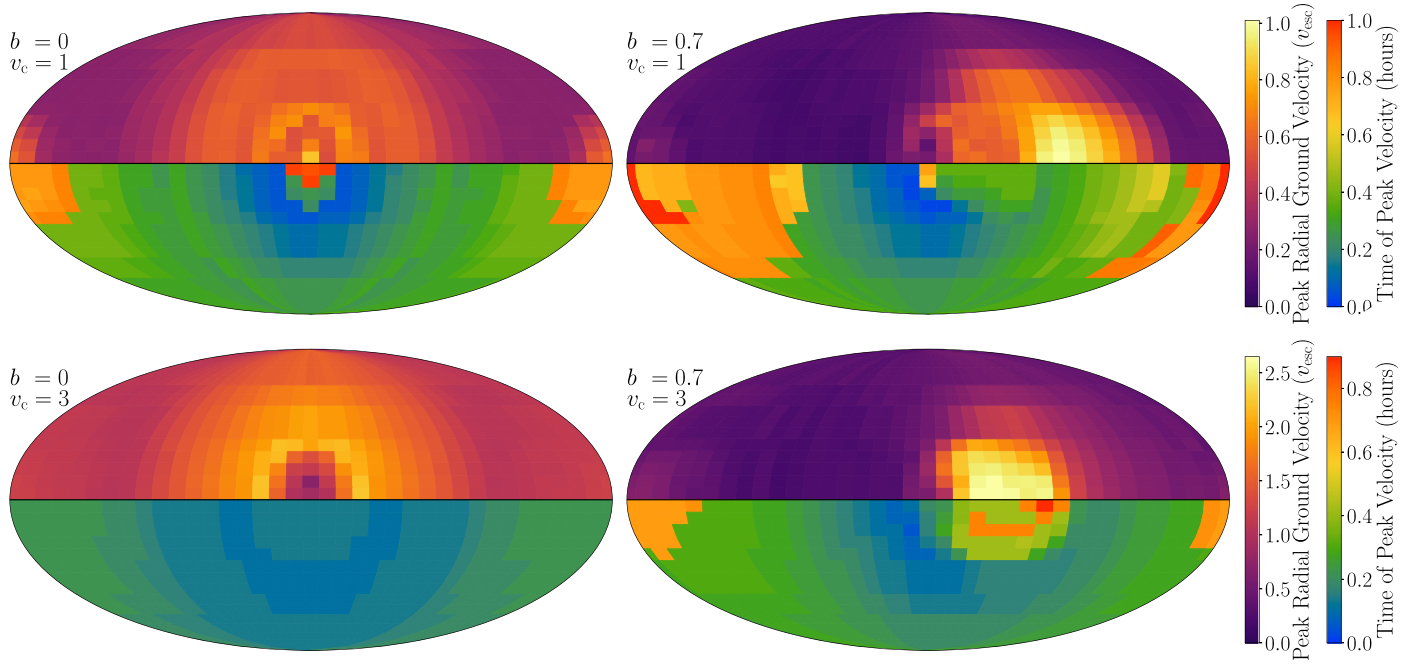

Figure 9. Maximum outward radial velocity of the outermost particles of the target's mantle (top hemispheres) and the times at which they occur (bottom hemispheres) for the four fiducial simulations, on a Mollweide projection with the point of contact at (0°, 0°) in the center, as described in Figure 8. The impacts are symmetric in latitude, so only one hemisphere is shown for each parameter. Note that the top, low-speed pair simulations share the same color bars that have different limits to those shared by the bottom, high-speed pair.

resulting in a slightly cooler, lower-density body than the default granite. The resulting loss was only 0.02 greater than the standard case's 0.52, with erosion occurring in the same locations at the same times, as was also seen in the temperature tests. This suggests that the atmospheric loss is not highly sensitive to mild changes in the target's material and precise internal structure.

3.4. Ground Speed

The one-dimensional estimates of Genda & Abe (2003, hereafter GA03) predict the local atmospheric loss for a given vertical ground speed. By defining the "ground" simulation particles as those in the outermost shell of the target's mantle, we can track their movement as shock waves (and the impactor itself) perturb them, as illustrated in Figure 8. We define longitude = 0° to be the point of contact with ±180° the antipode, and latitude = 0° is the impact ($z = 0$) plane. The maximum outward radial speed and the time at which it occurs at each location are given in Figure 9 for the four fiducial simulations.

The two head-on impacts are symmetric in longitude and show high peak speeds near the impact point and the antipode. For the slower of the two, the target recoils following the initial collision to shoot a plume of material back through the point of impact and a slightly less dramatic ejection at the antipode, causing the peak velocities in Figure 9 at those longitudes. Some earlier erosion around the antipode is also caused by the

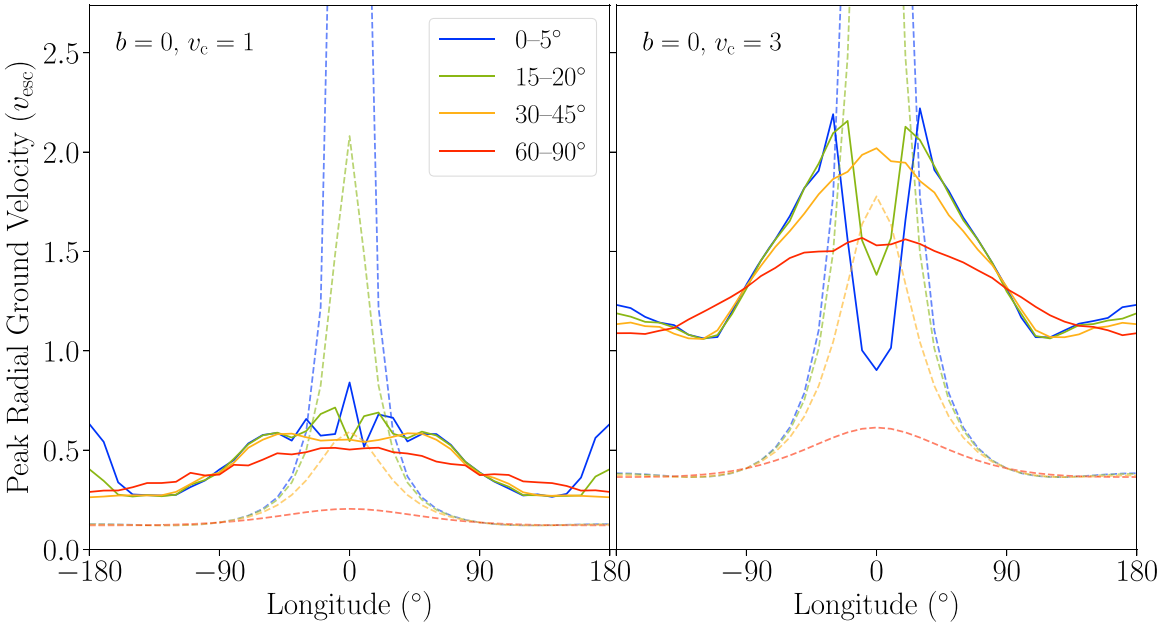

Figure 10. Maximum outward radial velocity of the outermost particles of the target's mantle as a function of longitude away from the impact point, in separate, similar-area |latitude| bins—effectively showing horizontal slices across Figure 9—for the two head-on fiducial simulations. The dashed lines show the estimated ground speeds at the same latitudes from Inamdar & Schlichting (2015), based on conserving a point-mass impactor's momentum in a spherical shock wave.

initial shock wave, which is the origin of the maximum velocities at most of the other longitudes and latitudes. As shown in Figure 9, this occurs a bit less than an hour before the peak recoil.

For the faster head-on collision, the impact is more destructive and no such bounce-back plume is seen. Instead, almost the entire surface is kicked immediately by the shock wave to faster than the escape speed, explaining the near-total erosion of atmosphere plus some lost mantle that was highlighted in Figure 4. In both head-on cases, the lower speeds at high latitudes simply reflect the rotational symmetry (as our planets are not spinning).

The two grazing collisions show similar behavior to each other with high speeds at positive longitudes, i.e., in the path of the impactor as it passes through the point of contact. The rest of the planet is hit by a shock wave, but not one nearly as strong as in the head-on cases, and with only a mild peak at the antipode. Unlike the head-on impacts, the grazing scenarios are not rotationally symmetric. Higher latitudes are less affected by the relatively small impactor and show little longitudinal variation.

In the slower grazing collision, the local loss around the impact site happens quickly, but the peak speeds everywhere else occur up to an hour later, corresponding to the initial fallback of some impactor fragments and the recoiling oscillation of the planet. In the faster grazing case, the shock wave quickly produces the peak speeds across most of the surface, with little significant fallback of fragments. The late times to the positive-longitude side of the impact site are less meaningful since most of this material is carried away at a roughly constant speed with the surviving impactor, slightly slower than the impactor's initial $3v_{esc}$. The peak antipode speeds are caused by the violent sloshing of the target as it begins to resettle following the shock.

Figure 10 shows a subset of the same peak ground speeds for comparison with those predicted by Inamdar & Schlichting (2015, hereafter IS15). These are independent of the impact parameter and so nominally correspond to head-on collisions. They assume that the impactor's momentum is transferred at the point of contact and is conserved with a constant speed of shocked material within the propagating spherical shock wave. While this inevitably overestimates the ground speed close to the point-mass impact, it also significantly underestimates the peak speed everywhere else and cannot reproduce the increase in speed at the antipode. This is unsurprising given their assumption that the entire volume of material traversed by the shock is all traveling at the same speed. In reality and in our simulations, the shock front moves much faster than the material behind it. The overprediction near the impact site has little effect on the results, as all atmosphere is removed there regardless, but the low speeds elsewhere lead to significant underestimates for the erosion.

IS15's model does not include the effects of gravity, the density profile, rarefaction waves after the shock reaches a surface, and the nonzero size and noninstant momentum transfer of the impactor. The internal structure of the planet changes dramatically as the large impactor plunges messily through the mantle; at high speeds, the impactor can even reach the core of the target well before the shock wave has reached the other side. It is possible that with additional modifications such models may be made useful, especially for fast, grazing impacts where the shock drives the majority of the loss in a simpler manner, though in that case an estimate for the fraction of the impactor's momentum that is transferred would also be required, dependent on the impact angle, speed, and planets' radii.

3.5. Local and Global Atmospheric Loss

Now that we have examined the ground speeds across the planet for the fiducial impacts and introduced 1D and analytical estimates for comparison, we show in Figure 11 the local atmospheric mass loss in each region for the four fiducial impacts.

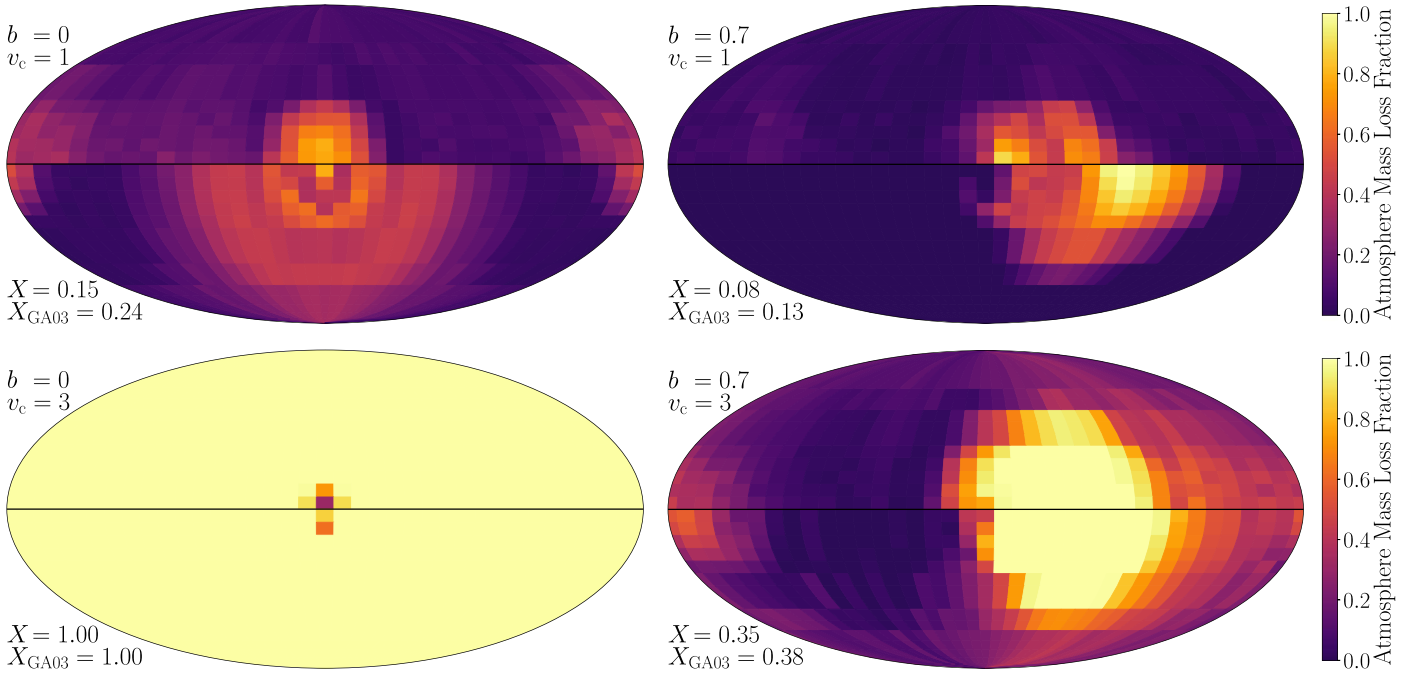

Figure 11. Loss fraction of local atmosphere (top hemispheres) for the four fiducial simulations, on a Mollweide projection as in Figure 9. The bottom hemispheres show the corresponding loss estimates from Genda & Abe (2003, GA03) using the peak ground speeds from our study that are shown in Figure 9. The annotations give the total loss, X, from the simulations globally for comparison with the total GA03 estimates.

The loss fractions broadly follow the distributions of peak ground speeds in Figure 9, and the GA03 results based on our peak speeds also match well the simulated loss in many places. Encouragingly, this implies that their 1D calculations and our SPH simulations reproduce similar results for a ground shock wave eroding the atmosphere above it once it arrives at the surface.

This is not always the case for the more complicated scenarios we are dealing with here. Perhaps the most significant reason is that for these estimates we have taken a single value for the peak ground speed at each location, whereas in reality the atmosphere can be ejected at many points in time—as was shown in Figure 9. We also cannot fix this simplification by applying GA03's estimates at, for example, all local-in-time maximum ground speeds, simply because the atmosphere must still be present above the ground for a shock to remove it. After the initial impact, some parts of the atmosphere could survive relatively undisturbed and be removed by subsequent shocks. However, other parts could be partially shocked away to fall back down at a later time, which may or may not coincide with later shocks. Thus, the assumption of a single ground speed could either over- or underestimate the actual local loss. We also used the radial ground speeds rather than the total, which, if used instead, produce slightly different qualitative results but very similar values for the total erosion.

Another important issue is the large size of the impactor and its complicated interaction with the target, compared with a simple point-mass explosion that would better produce loss just from ground shocks. Significant amounts of material can thus be ejected directly by the impactor plowing through the atmosphere and mantle, especially in grazing impacts.

Finally, there are the underlying assumptions made and discussed by GA03, such as their use of an ideal gas EOS and ignoring lateral motion of the atmosphere, both of which are likely to be more valid in their targeted regime of even thinner atmospheres. However, the fact that our simulations agree with theirs in many cases suggests that these simplifications are often not too important.

The overall results for the suite are presented in Figure 12, showing how the fraction of lost atmosphere varies with atmosphere mass, impact parameter, and speed. We find that, unsurprisingly, more atmosphere is usually lost from smaller atmospheres, more head-on collisions, and higher speeds. However, for slower collisions, the loss is not a monotonic function of the impact parameter, and a head-on collision does not cause the most erosion. By hitting slightly off-center, the impactor can deliver a strong shock through the planet while also encountering and eroding more atmosphere directly. Although more grazing impacts can directly remove even more local material, they fail to deposit enough energy into the shock to erode as much atmosphere on the far side.

Apart from this, by following the same ground-speed analysis as for the fiducial impacts, the GA03 estimates continue to reproduce the results well in most cases. As indicated by the ground speeds in Figure 10, the estimates from IS15 predict far less loss than most head-on collisions.

Bearing in mind that the results for the smallest atmospheres are not fully converged numerically, we find a relatively mild dependence on the initial atmosphere mass, partly depending on the specific scenario. This is supported by the good agreement of the GA03 estimates, which assumed a much thinner atmosphere than ours along the lines of Earth's present-day, $\sim 10^{-6} M_{\oplus}$ atmosphere.

In spite of the complicated details, including significant nonmonotonic dependence on the angle at low speeds, we find that a single parameter can be used to estimate the erosion from any scenario. Figure 13 shows the fraction of atmosphere lost, X, as a function of the modified specific impact energy, based on the specific energy used by Leinhardt & Stewart (2012) to predict disruption. We find that an additional factor of $(1-b)^2(1+2b)$ broadly accounts for the variation across the

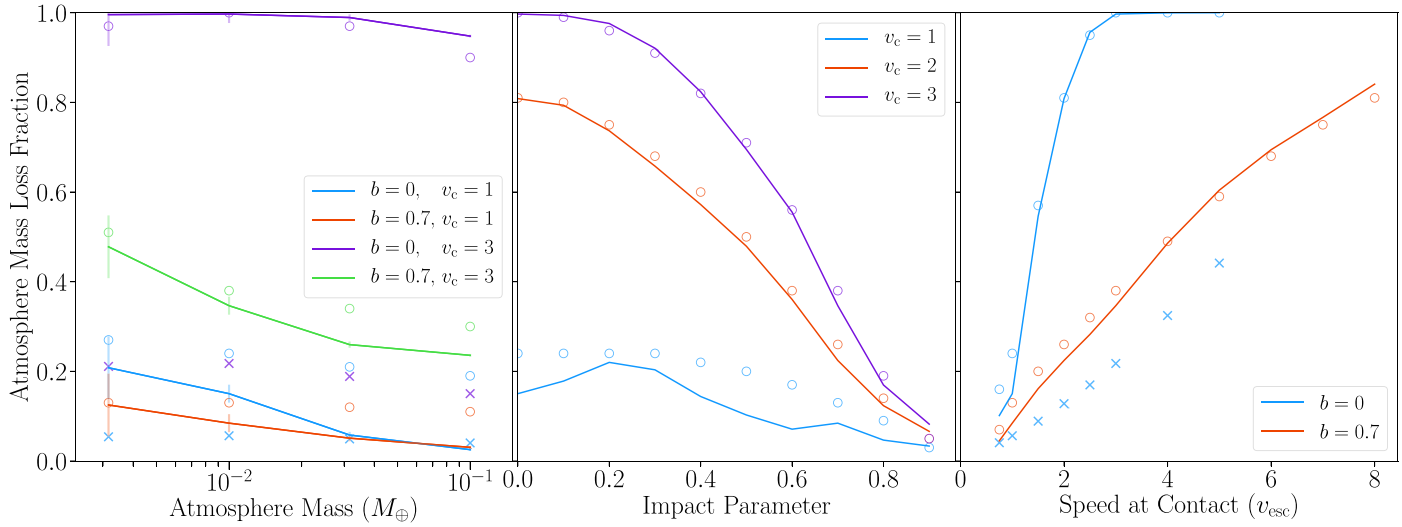

Figure 12. Lost mass fraction of the atmosphere for different atmosphere masses (left), in each of the fiducial impact scenarios; impact parameters (middle), for three different speeds; and speeds at contact (right), for each fiducial impact parameter; all with $\sim 10^7$ particles. The error bars in the left panel show the approximate, conservative uncertainty due to incomplete numerical convergence, which becomes significant for the lowest atmosphere mass. The circles show the corresponding Genda & Abe (2003) estimates based on the peak ground speeds. For the head-on collisions, the crosses show the Inamdar & Schlichting (2015) estimates based solely on the impactor's mass and speed relative to the target (their Figure 4).

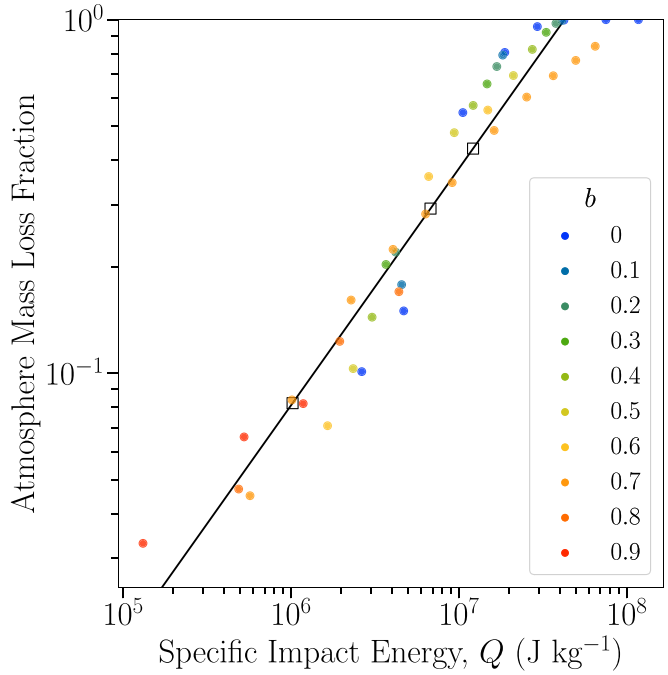

Figure 13. Lost mass fraction of the atmosphere for all the simulation scenarios as a function of their modified specific impact energy (Equation (1)), colored by their impact parameter. The black line shows our power-law fit (Equation (2)). The lower black square corresponds to the canonical Moon-forming impact (Canup & Asphaug 2001), and the other two to more recent, higher-energy scenarios (Ćuk & Stewart 2012; Lock et al. 2018). These results are also presented numerically in Table B1.

full range of head-on to highly grazing collisions:

$$Q = (1 - b)^2(1 + 2b)\frac{1}{2}\,\mu_r\,v_c^2\,\Big/M_{tot}, \tag{1}$$

where v_c is here the SI value not normalized by the escape speed and $\mu_r \equiv M_i M_t/M_{tot}$ is the reduced mass. The added term loosely accounts for the fractional volume of the two bodies that interacts: the volume of the target cap above the lowest point of the impactor at contact, plus the volume of the impactor cap below the highest point of the target, divided by the total volume, is $\frac{1}{4}[(R_t + R_i)^3\big/(R_t^3 + R_i^3)](1 - b)^2(1 + 2b)$ (see Appendix B). In reality, this is not the exact volume of material that actually interacts, especially for low-speed collisions or smaller impactors. Nonetheless, we find empirically that it allows a simple power-law fit for the loss fraction to be made in this regime, as shown in Figure 13:

$$X \approx 7.72 \times 10^{-6}(Q/\mathrm{J\,kg^{-1}})^{0.67}, \tag{2}$$

capped at one for total erosion. Note that the effects of changing the impact angle may have an additional dependence on the impactor's mass and radius, so from this initial study alone we can only be certain of this scaling law's applicability to bodies of this size. Its potential extrapolation to wider scenarios will be examined in a future study (J. A. Kegerreis et al. 2020, in preparation).

4. Conclusions

We have presented 3D simulations of giant impacts onto terrestrial planets with thin atmospheres. We explored a wide variety of speeds and impact angles, as well as a small range of atmosphere masses, and found a simple scaling law to estimate the fraction of atmosphere lost in this regime of approximately Earth-mass targets and Mars-mass impactors.

Several different processes can dominate the atmospheric loss in different scenarios, depending on, for example, whether the impactor can deliver a strong shock wave to remove atmosphere on the far side, or whether impactor fragments fall back after the initial collision. The interplay of these and other processes affects the total fraction of eroded atmosphere, the local distribution of where atmosphere is lost, and the time at which it is removed.

For head-on collisions, there is a rapid change with increasing impact speed from very little erosion to total loss. However, for grazing impacts with changing speed—or for fixed speeds with changing impact angle—there is a much

more gradual transition of partial erosion that also displays complex, nonmonotonic behavior at low to medium impact parameters.

We find that numerical convergence can require many more than 10^6 SPH particles, with a strong dependence on the specific impact scenario and the measurement in question, consistently with Kegerreis et al. (2019). The majority of our simulations used $\sim 10^7$ particles, which agree with simulations using $10^{7.5}$ and 10^8 on the fraction of atmosphere lost to within a few percent, with complete convergence in high-speed scenarios where more atmosphere is lost. Low-speed head-on collisions are particularly chaotic even at high resolution, making convergence harder to achieve. We conclude that bespoke convergence tests continue to be crucial for any project using planetary SPH simulations. That being said, our results provide the rough rule of thumb that about 10 layers of SPH particles are required to model the evolution of an atmosphere in these types of scenarios.

By tracking the ground movement throughout the simulations, we compared these 3D results with IS15's analytical estimates for the propagation of shocks from a giant impact, GA03's 1D models for local shock-driven erosion, and IS15's combined predictions for the global loss in a given scenario. IS15's ground velocities significantly underestimate the maximum ground speeds in head-on impacts owing to the dramatic deformation of the planet and violent post-impact oscillations. For the same reasons, their global predictions underestimate the total loss. Using our simulated ground speeds, GA03's estimates match the localized loss fractions well in most cases, especially when the direct encounter of the impactor with the atmosphere is not too important.

In the context of Earth and the canonical Moon-forming impact, only around 10% of the atmosphere would have been lost from the immediate effects of the collision. This suggests that the canonical impact itself cannot single-handedly explain the discrepancies between the volatile abundances of Earth and chondrites by eroding the early atmosphere, compared with alternative, more violent Moon-forming scenarios. However, the caveat of "immediate" erosion is important, because we have here only considered the direct, dynamical consequences of a giant impact. As examined by Biersteker & Schlichting (2019), the thermal effects of a giant impact heating the planet might erode comparable atmosphere to that ejected by shocks, though the volatile loss may not be that efficient even from a hot post-impact disk (Nakajima & Stevenson 2018). In addition, we took the simple approach here of defining "lost" atmosphere by particles that become gravitationally unbound, ignoring the fact that significant material can remain bound and still be ejected far away from the planet. In a real planetary system, whether by interaction with the solar wind or by leaving the target's Hill sphere of gravitational influence, much of the eroded but bound atmosphere could still be lost. As a separate point, Genda & Abe (2005) showed that the presence of an ocean can significantly enhance atmospheric loss, such that in the canonical Moon-forming scenario, closer to half the atmosphere could be immediately removed. Their models combined with our results could be used to estimate the amount of an ocean that would be removed in different scenarios, to constrain the extent of fractionation between volatiles. Future simulation studies could potentially resolve an ocean directly and test such erosion in more realistic detail.

The details of atmospheric erosion by giant impacts are complicated. These simulations provide a simple scaling law in this regime and form a starting point from which to explore the vast parameter space in detail. Promising targets for future study include investigations of different impactor and target masses; extensions to both more massive and even thinner atmospheres; the inclusion of an atmosphere on the impactor, as well as the target; and testing the dependence on the planets' materials, internal structures, and rotation rates. This way, robust scaling laws could be built up to cover the full range of relevant scenarios in both our solar system and exoplanet systems for the loss and delivery of volatiles by giant impacts.

We thank the anonymous reviewer for their constructive and insightful comments. The research in this paper made use of the SWIFT open-source simulation code (www.swiftsim.com, Schaller et al. 2018) version 0.8.5. This work was supported by the Science and Technology Facilities Council (STFC) grant ST/P000541/1 and used the DiRAC Data Centric system at Durham University, operated by the Institute for Computational Cosmology on behalf of the STFC DiRAC HPC Facility (www.dirac.ac.uk). This equipment was funded by BIS National E-infrastructure capital grant ST/K00042X/1, STFC capital grants ST/H008519/1 and ST/K00087X/1, STFC DiRAC Operations grant ST/K003267/1, and Durham University. DiRAC is part of the National E-Infrastructure. J.A.K. is supported by the ICC PhD Scholarships Fund and STFC grants ST/N001494/1 and ST/T002565/1. R.J.M. is supported by the Royal Society.

Software: SWIFT (www.swiftsim.com, Kegerreis et al. 2019; Schaller et al. 2016, version 0.8.5); SEAGen (pypi.org/project/seagen/).

Appendix A
Impact Initial Conditions

For each scenario, we choose the impact parameter, $b = \sin(\beta)$, and the speed, v_c, that the impactor would reach at first contact with the target, as illustrated in Figure 1. The input parameters for each simulation are also listed in Table A1. The distance between the body centers and the y position at contact are

$$r_c = R_i + R_t \tag{A1}$$

$$y_c = b r_c. \tag{A2}$$

The velocity at infinity,

$$v_{inf} = \sqrt{v_c^2 - 2\mu/r_c}, \tag{A3}$$

is zero for a parabolic orbit when $v_c = v_{esc}$, where $\mu = G(M_t + M_i)$ is the standard gravitational parameter and v_{esc} is the two-body escape speed. Note that for targets with atmospheres, we account for the mass of the atmosphere but ignore its thickness.

For elliptical or hyperbolic orbits, the speed and y position at any earlier time can be calculated using the vis-viva equation and conservation of angular momentum, where y is in the rotated reference frame where v is in the x-direction:

$$a = \left(\frac{2}{r_c} - \frac{v_c^2}{\mu}\right)^{-1} \tag{A4}$$

Table A1
Impact Parameter, Speed at Contact in Units of the Mutual Escape Speed, and Lost Mass Fraction of the Atmosphere for the Suite of Simulation Scenarios, as Presented in Figure 13

b	v_c	X	b	v_c	X	b	v_c	X
0.0	1	0.150	0.0	2	0.808	0.0	3	0.997
0.1	1	0.178	0.1	2	0.794	0.1	3	0.994
0.2	1	0.220	0.2	2	0.737	0.2	3	0.976
0.3	1	0.203	0.3	2	0.658	0.3	3	0.921
0.4	1	0.144	0.4	2	0.572	0.4	3	0.824
0.5	1	0.103	0.5	2	0.479	0.5	3	0.695
0.6	1	0.071	0.6	2	0.360	0.6	3	0.555
0.7	1	0.084	0.7	2	0.224	0.7	3	0.346
0.8	1	0.047	0.8	2	0.123	0.8	3	0.170
0.9	1	0.033	0.9	2	0.066	0.9	3	0.082
0.0	0	0.101	0.7	0	0.045	0.7	6	0.694
0.0	1	0.546	0.7	1	0.161	0.7	7	0.767
0.0	2	0.956	0.7	2	0.282	0.7	8	0.841
0.0	4	1.000	0.7	4	0.486			
0.0	5	1.000	0.7	5	0.604			

$$v = \sqrt{\mu\left(\frac{2}{r} - \frac{1}{a}\right)} \tag{A5}$$

$$y = \frac{y_c v_c}{v}, \tag{A6}$$

where a is the semimajor axis, which is negative for hyperbolic orbits, and v_c is the speed at contact.

In order to rotate the coordinate system such that, at contact, the velocity will be in the x-direction (a purely aesthetic choice), we first find the periapsis, r_p, and then the eccentricity, e. Taking the vis-viva equation at periapsis and using Equation (A6) to eliminate the speed gives

$$r_p^2 - a\, r_p + \frac{a v_c^2 y_c^2}{2\mu} = 0 \tag{A7}$$

$$r_p = \frac{a \pm \sqrt{a^2 - \frac{2 a v_c^2 y_c^2}{\mu}}}{2} \tag{A8}$$

$$e = 1 - r_p/a, \tag{A9}$$

which allows calculation of the true anomaly (in this case its complement, θ) and the angle of the velocity away from the radial vector, α':

$$\theta = \cos^{-1}\left(\frac{1 - \frac{a(1-e^2)}{r}}{e}\right) \tag{A10}$$

$$\alpha' = \sin^{-1}\left(\frac{a^2(1-e^2)}{2ar - r^2}\right). \tag{A11}$$

The final angle needed to rotate the starting x, y, and v is

$$\phi = \alpha' - \theta_c + \theta - \sin^{-1}\frac{y}{r}, \tag{A12}$$

where the c subscript again signifies at contact. In the special case of a parabolic orbit, the contact and initial speeds and angles can be calculated directly:

$$v = \sqrt{2\mu/r} \tag{A13}$$

$$\theta = \pi - \cos^{-1}\left(\frac{y_c^2 v_c^2}{\mu r}\right) \tag{A14}$$

$$\alpha' = \theta_c/2, \tag{A15}$$

followed by the same rotation by ϕ.

The time taken from the initial position to contact, t_c, can be found by using the eccentric anomaly, E,

$$E_{ell} = \cos^{-1}\frac{e + \cos\theta}{1 + e\cos\theta} \tag{A16}$$

$$E_{hyp} = \cosh^{-1}\frac{e + \cos\theta}{1 + e\cos\theta} \tag{A17}$$

$$E_{par} = \tan\frac{\theta}{2}, \tag{A18}$$

and mean anomaly, M,

$$M_{ell} = E - e\sin E \tag{A19}$$

$$M_{hyp} = -E + e\sinh E \tag{A20}$$

$$M_{par} = E + E^3/3, \tag{A21}$$

to find the time since periapsis, t_p,

$$t_{p,ell,hyp} = \sqrt{\frac{|a|^3}{\mu}}\, M \tag{A22}$$

$$t_{p,par} = \sqrt{\frac{2\, r_p^3}{\mu}}\, M. \tag{A23}$$

Then, $t_c = t_p(\theta) - t_p(\theta_c)$.

For a radial orbit, the time until the point masses would contact, t_p', is

$$t'_{p,par} = \sqrt{\frac{2r^3}{9\mu}} \tag{A24}$$

$$t'_{p,ell} = \frac{\sin^{-1}(\sqrt{wr}) - \sqrt{wr(1-wr)}}{\sqrt{2\mu w^3}} \tag{A25}$$

$$t'_{p,hyp} = [\sqrt{(|w|r)^2 + |w|r} \tag{A26}$$

$$\frac{-\ln(\sqrt{|w|r} + \sqrt{1 + |w|r})]}{\sqrt{2\mu|w|^3}}, \tag{A27}$$

where w is the standard constant

$$w = \frac{1}{r} - \frac{v^2}{2\mu}, \tag{A28}$$

and we can extract t_c as before.

For these simulations, we choose the time until contact to be 1 hr to determine the initial separation and positions. The equations for the mean anomaly in terms of the eccentric anomaly do not have analytical inversions, so we simply iterate an estimate of the initial separation, r, until we obtain the desired t_c.

Appendix B
Approximate Interacting Volume

For this crude estimate of the fractional volume of the target and impactor that interacts in a grazing collision, we consider the situation illustrated in Figure 1 by the target and dotted-line impactor at contact. We assume that the relevant portion of the

target is the spherical cap above the horizontal plane set by the lowest point of the impactor at contact. The relevant portion of the impactor is that below the horizontal plane set by the highest point of the target.

The volume of a spherical cap with height d is

$$V_{\rm cap}(R, d) = \frac{\pi}{3} d^2 (3R - d), \tag{B1}$$

where R is the radius of the sphere. In our scenario, the heights of both caps are

$$d = R_{\rm tot} - R_{\rm tot} \sin\beta = R_{\rm tot}(1 - b), \tag{B2}$$

where $R_{\rm tot} = R_{\rm t} + R_{\rm i}$ is the distance between the two centers.

The interacting volume is then the sum of the target and impactor caps:

$$\begin{aligned} V &= V_{\rm cap}(R_{\rm t}, d) + V_{\rm cap}(R_{\rm i}, d) \\ &= \frac{\pi}{3} d^2 [(3R_{\rm t} - d) + (3R_{\rm i} - d)] \\ &= \frac{\pi}{3} d^2 [3R_{\rm tot} - 2d] \\ &= \frac{\pi}{3} R_{\rm tot}^2 (1 - b)^2 [3R_{\rm tot} - 2R_{\rm tot}(1 - b)] \\ &= \frac{\pi}{3} R_{\rm tot}^3 (1 - b)^2 (1 + 2b). \end{aligned} \tag{B3}$$

Dividing by the total volume of both spheres gives the fractional volume:

$$f_{\rm V} = \frac{1}{4} \frac{R_{\rm tot}^3}{R_{\rm t}^3 + R_{\rm i}^3} (1 - b)^2 (1 + 2b). \tag{B4}$$

If the impactor is small and the angle is low, then the top of the impactor drops below the top of the target when $d > 2R_{\rm i} \rightarrow b < 1 - 2R_{\rm i}/R_{\rm tot}$. In this case, the full sphere of the impactor should be included and the small target cap above the top of the impactor should be removed. However, this has a negligible effect for large impactors because the discrepancies in the impactor and target volumes almost cancel out. It starts to become relevant as the impactor's radius falls to below half of the target's radius, but even for $R_{\rm i} = 0.3\,R_{\rm t}$ the difference is still only 15%. The large impactors in this study have $R_{\rm i} \approx 0.6\,R_{\rm t}$. Future work should determine whether this scaling law must be modified for different bodies.

It is debatable whether this volume is a sensible estimate for low-angle collisions, where it could be argued that the entirety of both bodies is involved. We also note that this is not the actual intersection of two spheres if they were to pass through each other. Under the assumption that the impactor moves in a straight line, which is valid for high-speed collisions, the relevant volume would be given by the intersection of a sphere and a cylinder. However, this is much more difficult to calculate and seems unlikely to provide much better results in what would still be a highly simplified model of a real collision, which involves dramatic distortion of the colliding "spheres." Therefore, we stick to the convenient expression and empirical adequacy of Equation (B4).

ORCID iDs

J. A. Kegerreis https://orcid.org/0000-0001-5383-236X
V. R. Eke https://orcid.org/0000-0001-5416-8675
R. J. Massey https://orcid.org/0000-0002-6085-3780
L. F. A. Teodoro https://orcid.org/0000-0002-8346-0138

References

Balsara, D. S. 1995, JCoPh, 121, 357
Benz, W., & Asphaug, E. 1999, Icar, 142, 5
Biersteker, J. B., & Schlichting, H. E. 2019, MNRAS, 485, 4454
Bonomo, A. S., Zeng, L., Damasso, M., et al. 2019, NatAs, 3, 416
Canup, R. M., & Asphaug, E. 2001, Natur, 412, 708
Chambers, J. E. 2001, Icar, 152, 205
Ćuk, M., & Stewart, S. T. 2012, Sci, 338, 1047
Fressin, F., Torres, G., Charbonneau, D., et al. 2013, ApJ, 766, 81
Genda, H., & Abe, Y. 2003, Icar, 164, 149
Genda, H., & Abe, Y. 2005, Natur, 433, 842
Halliday, A. N. 2013, GeCoA, 105, 146
Hosono, N., Iwasawa, M., Tanikawa, A., et al. 2017, PASJ, 69, 26
Hubbard, W. B., & MacFarlane, J. J. 1980, JGR, 85, 225
Hwang, J., Chatterjee, S., Lombardi, J. J., Steffen, J. H., & Rasio, F. 2018, ApJ, 852, 41
Inamdar, N. K., & Schlichting, H. E. 2015, MNRAS, 448, 1751
Kegerreis, J. A., Eke, V. R., Gonnet, P., et al. 2019, MNRAS, 487, 5029
Kegerreis, J. A., Teodoro, L. F. A., Eke, V. R., et al. 2018, ApJ, 861, 52
Leinhardt, Z. M., & Stewart, S. T. 2012, ApJ, 745, 79
Liu, S.-F., Hori, Y., Lin, D. N. C., & Asphaug, E. 2015, ApJ, 812, 164
Lock, S. J., Stewart, S. T., Petaev, M. I., et al. 2018, JGRE, 123, 910
Lopez, E. D., & Fortney, J. J. 2014, ApJ, 792, 1
Lopez, E. D., Fortney, J. J., & Miller, N. 2012, ApJ, 761, 59
Massol, H., Hamano, K., Tian, F., et al. 2016, SSRv, 205, 153
Melosh, H. J. 2007, M&PS, 42, 2079
Nakajima, M., & Stevenson, D. J. 2018, E&PSL, 487, 117
Petigura, E. A., Howard, A. W., & Marcy, G. W. 2013, PNAS, 110, 19273
Raymond, S. N., O'Brien, D. P., Morbidelli, A., & Kaib, N. A. 2009, Icar, 203, 644
Sakuraba, H., Kurokawa, H., & Genda, H. 2019, Icar, 317, 48
Schaller, M., Gonnet, P., Chalk, A. B. G., & Draper, P. W. 2016, in Proc. Platform for Advanced Scientific Computing Conf. 16, 1, https://dl.acm.org/doi/abs/10.1145/2929908.2929916
Schaller, M., Gonnet, P., Draper, P. W., et al. 2018, SWIFT: SPH With Inter-dependent Fine-grained Tasking, v. 0.8.5, Astrophysics Source Code Library, ascl:1805.020
Schlichting, H. E., & Mukhopadhyay, S. 2018, SSRv, 214, 34
Schlichting, H. E., Sari, R., & Yalinewich, A. 2015, Icar, 247, 81
Shuvalov, V. 2009, M&PS, 44, 1095
Stewart, S. T., Davies, E. J., Duncan, M. S., et al. 2019, arXiv:1910.04687
Tillotson, J. H. 1962, General Atomic Report, GA-3216, 141
Tucker, J. M., & Mukhopadhyay, S. 2014, E&PSL, 393, 254
Zahnle, K. J., & Catling, D. C. 2017, ApJ, 843, 122
Zahnle, K. J., Gacesa, M., & Catling, D. C. 2019, GeCoA, 244, 56